

Flexible, Biodegradable, and Wireless Magnetolectric Paper for Simple In Situ Personalization of Bioelectric Implants

Jun Kyu Choe, Suntae Kim, Ah-young Lee, Cholong Choi, Jae-Hyeon Cho, Wook Jo, Myung Hoon Song,* Chaenyung Cha,* and Jiyun Kim*

Bioelectronic implants delivering electrical stimulation offer an attractive alternative to traditional pharmaceuticals in electrotherapy. However, achieving simple, rapid, and cost-effective personalization of these implants for customized treatment in unique clinical and physical scenarios presents a substantial challenge. This challenge is further compounded by the need to ensure safety and minimal invasiveness, requiring essential attributes such as flexibility, biocompatibility, lightness, biodegradability, and wireless stimulation capability. Here, a flexible, biodegradable bioelectronic paper with homogeneously distributed wireless stimulation functionality for simple personalization of bioelectronic implants is introduced. The bioelectronic paper synergistically combines i) lead-free magnetolectric nanoparticles (MENs) that facilitate electrical stimulation in response to external magnetic field and ii) flexible and biodegradable nanofibers (NFs) that enable localization of MENs for high-selectivity stimulation, oxygen/nutrient permeation, cell orientation modulation, and biodegradation rate control. The effectiveness of wireless electrical stimulation *in vitro* through enhanced neuronal differentiation of neuron-like PC12 cells and the controllability of their microstructural orientation are shown. Also, scalability, design flexibility, and rapid customizability of the bioelectronic paper are shown by creating various 3D macrostructures using simple paper crafting techniques such as cutting and folding. This platform holds promise for simple and rapid personalization of temporary bioelectronic implants for minimally invasive wireless stimulation therapies.

alternative to traditional pharmaceuticals.^[1] For example, these implants can promote and modulate cellular activities to facilitate tissue regeneration (e.g., peripheral nerve and bone),^[2–4] regulate heart beating,^[5] or treat neurodegenerative diseases such as Parkinson's disease, Alzheimer's disease, and paralysis.^[6–9] However, most of the state-of-the-art bioelectronic implants require rigid and bulky electronics that are mechanically incompatible with the delicate structure of nerves and other tissues, leading to potential tissue damage and foreign body reactions. In addition, the need for wire connections, battery replacement, and post-treatment removal surgeries can raise the risk of infection and make clinical treatments complex.

To address these issues, recent studies have delved into the use of flexible electronics^[10–17] and wireless electrical stimulation^[18–24] to provide safer tissue interactions and facilitate clinical management. These flexible implants can usually exploit thin film form factor^[11,16,20] which further allows the structure to conform to intricate surfaces of the tissues, and biodegradable materials^[12,18,23] which then naturally disintegrate in the body after operating a designated period of time.

However, these implants operate through system-level integration of components (e.g., capacitor, diode, antenna, substrate, and electrode) that make specific fragmentary functional contributions to a task in their respective assigned locations. Therefore, since cohesive connections between the components are critical for operation, any minor damage to a single component can cause the entire device to malfunction. Moreover, adjusting the micro- or macro-structural design and miniaturizing the implants while maintaining cohesive integrity is technically complex, costly, or intrinsically limited. Therefore, personalizing the implants to each unique clinical and physical circumstance for minimally invasive treatment remains a challenge. Furthermore, this restricted tunability may limit potential applications, especially for therapies that require high-selectivity electrical stimulation or have confined or complex implantable space.

As another possibility, magnetolectric smart composite materials that can generate localized electric fields in response to external magnetic field have gained considerable interests due to the

1. Introduction

Bioelectronic implants that deliver electrical stimulation have shown great promise in the field of electrotherapy as an

J. K. Choe, S. Kim, A.-young Lee, C. Choi, J.-H. Cho, W. Jo, M. H. Song, C. Cha, J. Kim

Department of Materials Science and Engineering
 Ulsan National Institute of Science and Technology (UNIST)
 Ulsan 44919, Republic of Korea

E-mail: mhsong@unist.ac.kr; ccha@unist.ac.kr; jiyunkim@unist.ac.kr

J. Kim

Center for Multidimensional Programmable Matter
 Ulsan National Institute of Science and Technology
 Ulsan 44919, Republic of Korea

The ORCID identification number(s) for the author(s) of this article can be found under <https://doi.org/10.1002/adma.202311154>

DOI: 10.1002/adma.202311154

minimally invasive nature of wireless magnetic fields and ease of implementation at smaller scales owing to the inherent functionality of the material itself.^[25] However, the current state-of-the-art magnetoelectric composites mostly incorporate substantial quantities of lead-based materials, such as lead zirconate titanate (PZT) and lead magnesium niobate-lead titanate. For example, a common magnetoelectric composite comprises a sub-centimeter bi-layered laminate configuration of PZT and an amorphous metallic glass, Metglas, bonded together using epoxy.^[21,26] This approach can raise safety concerns, mainly attributed to the lead content in PZT and mismatch in structure and mechanical properties with biological tissues. As a potential solution, lead-free magnetoelectric nanoparticles (MENs) have been explored for biocompatible wireless stimulations within deep tissues, including brain stimulations.^[27] However, prevalent approach involves direct injection of MENs with a dosage corresponding to the body weight of an animal,^[28,29] elevating the risk of inessential overdosing that could compromise the ability of MENs to precisely stimulate localized areas owing to their nanoscale and potentially induce long-term cytotoxic effects. Therefore, ensuring controlled and targeted delivery of MENs to specific body sites remains a challenge.

Here, we introduce a flexible, biomimetic, lightweight, and biodegradable bioelectronic paper that can be cut and tailored post-fabrication while retaining functionalities, allowing for simple and rapid production of bioelectronic implants of various sizes, shapes, and micro- and macro-structures. The overview of the bioelectronic paper is shown in **Figure 1a**. To achieve this, we employ a material-based approach to create dispersed electrical stimulation capabilities throughout the device, leveraging the advantages of nanoscale functional materials that constitute our entire platform: i) lead-free core-shell MENs and ii) flexible, biomimetic, and biodegradable nanofibers (NFs) that carries the MENs. The lead-free MEN consists of coupled CoFe_2O_4 (CFO) magnetostrictive core, which transduces external magnetic field into strain, and BaTiO_3 (BTO) piezoelectric shell, which transduces applied strain into electricity (**Figure 1b**; see **Figure S1**, Supporting Information for the transduction mechanism). This core-shell structure increases coupling interface (and thus mechanical transmission) between the two materials when compared to other simply mixed structures,^[30] thus allowing efficient wireless electrical stimulation with a mild external magnetic field (see **Figure S1**, Supporting Information). In addition, the magnetic-responsive MEN can deliver electrical stimulation deeper into tissue without creating drastic stress or heat, as opposed to other wireless stimulation technologies that use ultrasound^[19] or electromagnetic field,^[13] and avoid potential health risks associated with other conventional lead-based magnetoelectric implants.^[19,21,22,31]

Next, the NF template enables localization of the MEN for efficient high-selectivity electrical stimulation, oxygen and nutrients permeation through the porous microstructure, and cell-to-cell connectivity control with tunable degree of NF alignment (**Figure 1c**). The NF consists of poly(lactic-co-glycolic acid) (PLGA), one of the most attractive biocompatible polymers approved by the FDA^[32] providing softness, flexibility, and tunable biodegradability. Furthermore, the NF template allows for straightforward scaling and structure morphing with a limitless variety of designs, similar to origami and kirigami paper arts that

use thin paper sheets.^[33–35] Through the combination of these nanoscale unit materials, the bioelectronic paper with a favorable low area density of 0.03 g cm^{-2} could offer safe, efficient, and controllable wireless cell modulations, all of which can be retained during cutting or folding of the platform for simple personalization.

We show facile synthesis of our bioelectronic platform using hydrothermal and sol-gel growth for lead-free MEN implementation, followed by electrospinning of PLGA solution blended with MEN. We then demonstrate in vitro proof-of-principle that our platform can enhance neuronal differentiation of neuron-like PC12 cells with wireless electrical stimulation, and manipulate their directional morphology by controlling the NF orientation. Last, we show extensive 3D macrostructure and scale programmability achieved through the combination of simple rolling, cutting, and folding of the thin film platform.

Figure 1d shows the new scheme we plan to establish using our platform. The bioelectronic paper, featuring both homogeneously distributed wireless stimulation and cell alignment controllability (**Figure 1d(i)**), can be simply personalized for various clinical and physical situations (**Figure 1d(ii–iv)**). Then, followed by wireless treatment (**Figure 1d(v)**), the bioelectronic paper can be biodegraded with a controlled dissolution rate, which eliminates the requirement of additional removal surgery after the desired treatment period (**Figure 1d(vi)**). We expect that these results with unprecedented design flexibility can lay a foundation for the low-cost, simple, and rapid personalization of temporary bioelectronic implants for minimally invasive wireless stimulation therapies.

2. Results and Discussion

2.1. Magnetoelectric Nanoparticles

The MEN was synthesized through a wet chemical method as shown in **Figure 2a**, due to the simplicity, tunability, and cost-effectiveness of the process.^[36] First, CFO magnetostrictive nanoparticles were prepared by hydrothermal reaction of Co^{2+} and Fe^{3+} precursors. The fabricated CFO showed spherical morphologies with a size of $19.1 \pm 3.8 \text{ nm}$ (**Figure S2a**, Supporting Information). Then, to form BTO shell structures on CFO nanoparticles, Ba^{2+} and Ti^{4+} precursors were introduced to the as-prepared CFO nanoparticles followed by sol-gel reaction and calcination steps (see Experimental Section “Synthesis of CFO nanoparticles” and “Synthesis of CFO@BTO Core/Shell MENs” for more detail). The resulting CFO@BTO showed similar spherical morphologies with a size of $21.3 \pm 4.7 \text{ nm}$ (**Figure 2b(i)**; **Figure S2b**, Supporting Information).

Figure 2b(ii) shows the energy-dispersive X-ray spectroscopy (EDS) results confirming evenly distributed constituent elements and core/shell structure of the CFO@BTO with Ba and Ti shell elements having larger distributed area than the Co and Fe core elements ($\approx 2.2 \text{ nm}$ in thickness). In **Figure 2c**, the ratios of the constituent elements were measured using an inductively coupled plasma-optical emission spectrometry (ICP-OES). The elemental ratio between Co and Fe (33.6:66.4), and the ratio between Ba and Ti (50.7:49.3) were comparable to the ratios of the cations that compose CFO (1:2) and BTO (1:1) respectively. The CFO to

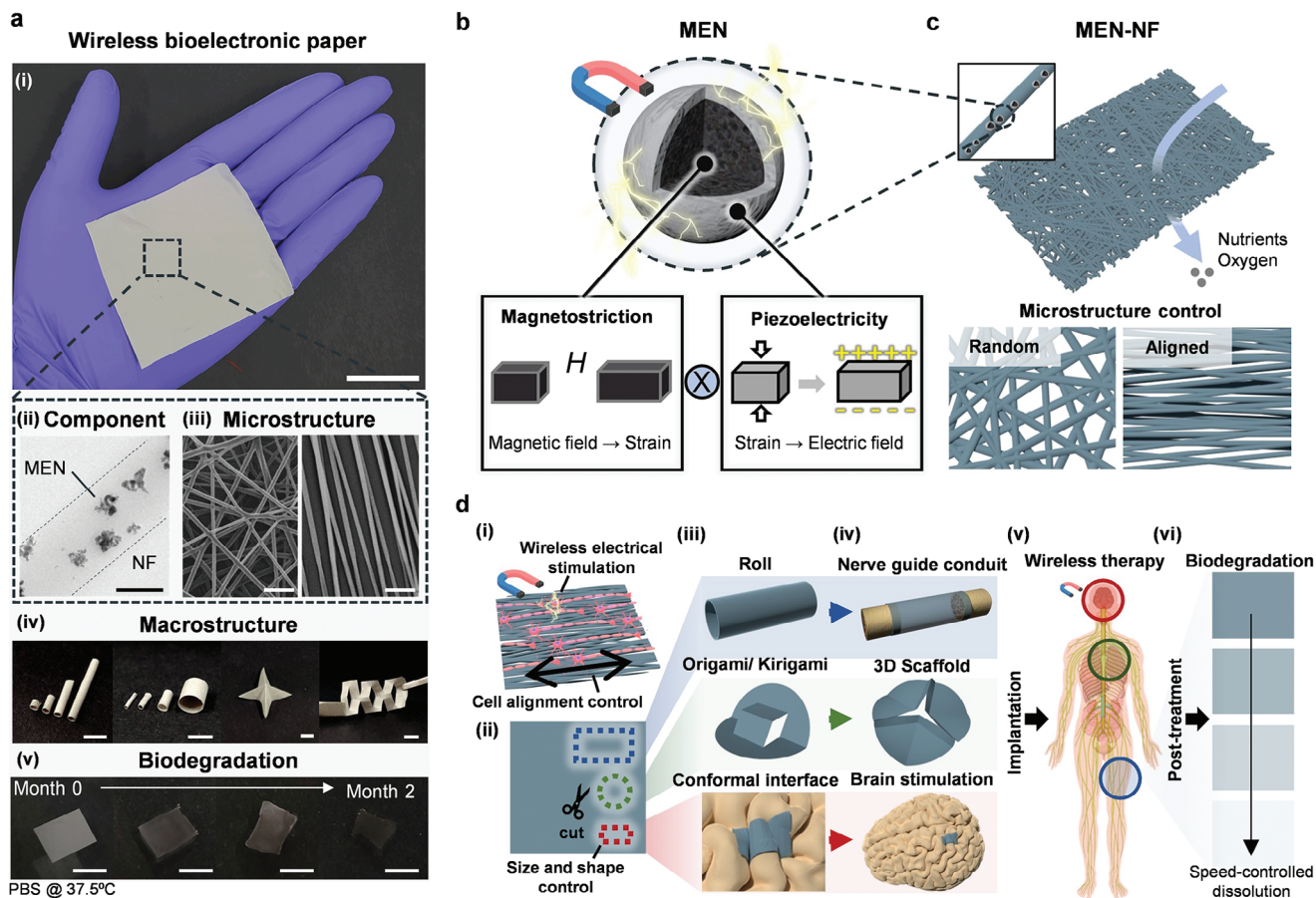


Figure 1. Overview of the implantable, wireless bioelectronic paper. a) i) Photograph of a bioelectronic paper (thickness $\approx 50 \mu\text{m}$; scale bar, 3 cm) fabricated via ii) integrating magnetolectric nanoparticles (MEN) into electrospun biodegradable nanofiber (NF; image obtained by TEM; scale bar, 500 nm). iii) The microstructure of the bioelectronic paper can be designed to random or aligned fiber orientation (images obtained by SEM; scale bars, 5 μm). iv) Photographs of the bioelectronic paper tailored into various macrostructures and scales using simple rolling, origami, and kirigami techniques (scale bars, 5 mm). v) Sequential images showing dissolution of the bioelectronic paper during immersion in PBS at 37.5 $^{\circ}\text{C}$ (scale bars, 1 cm). b) Schematic illustration of MEN synthesized in core/shell structure that couples magnetostrictive core that transduces magnetic field into local strain and piezoelectric shell that transduces strain into electric field. c) The MEN-integrated NF (MEN-NF) has high porosity that allows permeation of small molecules and controllability in microstructural fiber orientations. d) Schematic illustration of newly proposed scheme leveraging the bioelectronic paper. i) The bioelectronic paper can deliver wireless electrical stimulation and control cell alignment, which functions are retained under ii) cutting of the bioelectronic paper into various sizes and shapes. iii) Diverse macrostructures or plain sheets that conform to complex surfaces are simply obtained from a single paper, which could serve in future applications, for example, as iv) nerve guide conduit, 3D scaffold, and brain stimulation platform. v) The bioelectronic paper personalized to fit specific clinical and physical environments is implanted for minimally invasive wireless electrical therapy. vi) After a desired period of treatment, the bioelectronic paper dissolves into the body eliminating the need for surgical extraction.

BTO atomic ratio was 77.2: 22.8, which clarifies the smaller thickness of the BTO shell compared to the radius of the CFO core.

The crystalline structures of the CFO@BTO MENs were characterized using X-ray diffraction (XRD) analysis (Figure 2d). The bottom XRD pattern belonged to a spinel structure CFO (COD#1 533 163), and after incorporating the shell elements, the XRD pattern (top) showed new additional peaks that belonged to perovskite structure BTO (COD#1 507 756), indicating successful coating of BTO on CFO nanoparticles. There were no XRD-detectable impurities or intermediate phases.

Next, to investigate the electrical response of MENs under an applied magnetic field, the direct magnetolectric coupling coefficient $\alpha_{\text{ME}} = \delta E \delta H^{-1}$ was measured using a widely used lock-in technique^[37] (see Experimental Section “Magnetolectric

coefficient characterization” for more detail). In Figure 2e, The α_{ME} showed hysteretic behavior with coercive fields of -0.41 and 0.20 kOe , and remanent α_{ME} values of -0.47 and $1.1 \text{ mV cm}^{-1} \text{ Oe}^{-1}$, which behavior is in accordance with the ferrimagnetic nature of the spinel ferrite component.^[38] Also, the α_{ME} varied nonlinearly in response to the DC field, as is typically expected for magnetolectric materials.^[39] The maximum α_{ME} value was $2.45 \text{ mV cm}^{-1} \text{ Oe}^{-1}$, which was similar to other reported values.^[37]

To evaluate biocompatibility of the MENs, in vitro cytotoxicity tests of neuron-like PC12 cells were performed on tissue culture flasks with MEN-dispersed culture medium at concentrations up to 50 mg mL^{-1} . As shown in Figure 2f, the MENs exhibited good biocompatibility with $>90\%$ cell viability at concentrations

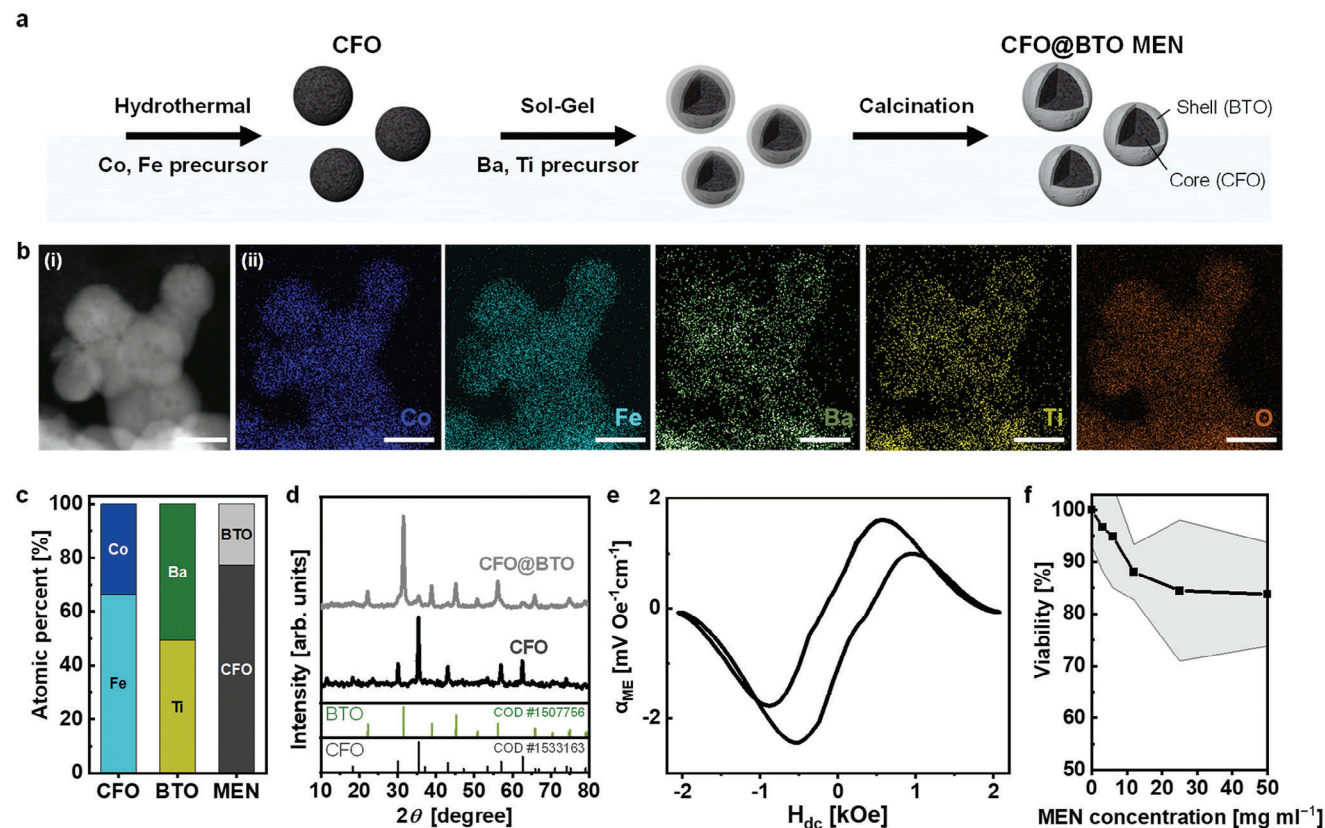


Figure 2. Synthesis and characterization of core/shell CFO@BTO MENs. a) Schematic diagram of synthesizing the core/shell CFO@BTO MEN. b) i) TEM image of MEN and ii) corresponding EDS mapping images (scale bars, 20 nm). c) ICP-OES analysis results showing atomic percent of constituent elements in CFO core and BTO shell, and core/shell ratio in MEN. d) XRD patterns for CFO and CFO@BTO MEN with the standard card COD #1 533 163 and COD #1 507 756 corresponding to the CFO and BTO respectively. e) magneto-electric coupling coefficient α_{ME} as a function of DC magnetic field. f) PC12 cell viability at day 1 according to MEN concentration in culture media. Shaded area represents the standard deviation.

up to $\approx 10 \text{ mg mL}^{-1}$. Furthermore, cell viability was well maintained, exceeding 80%, even at high MEN concentrations ranging from 10 to 50 mg mL^{-1} . Collectively, these results suggest that the core-shell CFO@BTO MENs were successfully synthesized, with adequate magneto-electric effect and biocompatibility for potential wireless electrical signaling applications in biological systems.

2.2. MEN-Integrated PLGA Nanofiber

While MENs have the capability to control electro-microenvironments with external magnetic fields, their high mobility caused by their nanoscale structure could complicate the accurate localization of their position. Therefore, although MEN has been previously injected in various environments including tissues^[40–42] and blood vessels,^[28] delivering MENs by themselves poses a risk of unnecessary overdosing, which could mud their capability to localize electrical stimulation for high-selectivity electrical stimulation and possibly show long-term cytotoxic behavior.

First, we resolve this issue by implementing biomimetic PLGA nanofiber to create MEN-integrated nanofiber (MEN-NF) bio-electronic paper. The NF template is distinguished by its flex-

ibility, high surface-to-volume ratio, and highly porous fibrous structure, which resembles the features of the native extracellular matrix (ECM). As shown in **Figure 3a**, The MEN-NF was fabricated through electrospinning of a blending solution of 1,1,1,3,3,3-hexafluoro-2-propanol, MEN (20 mg mL^{-1}), gelatin (1 wt%), and PLGA (15 wt%) at a high DC voltage (14 kV) that is either connected to a plate collector (for random structure NF) or a rotating drum collector (for aligned structure NF). For more details regarding the fabrication of MEN-NF, see Experimental Section “Preparation of MEN-NF bioelectronic paper.” The microstructures of the electrospun MEN-NF were characterized using scanning electron microscopy (SEM), which results clearly demonstrated beads-free NFs with the microstructure design tunability to either random (**Figure 3b(i)**) or aligned orientation (**Figure 3b(ii)**). The diameter of the aligned MEN-NF ($448 \pm 11 \text{ nm}$) was lower than that of random MEN-NF ($620 \pm 17 \text{ nm}$) which could be attributed to the higher level of stretching placed on NF during the collection with high-speed rotating drum collector (**Figure S3**, Supporting Information).

Then, we validated the successful integration of MENs within the PLGA NF via the transmission electron microscopy (TEM) results shown in **Figure 3c**. The fabricated MEN-NF bio-electronic paper had uniform light grey color, in contrast to the white NF without MENs, which further indicated the presence of

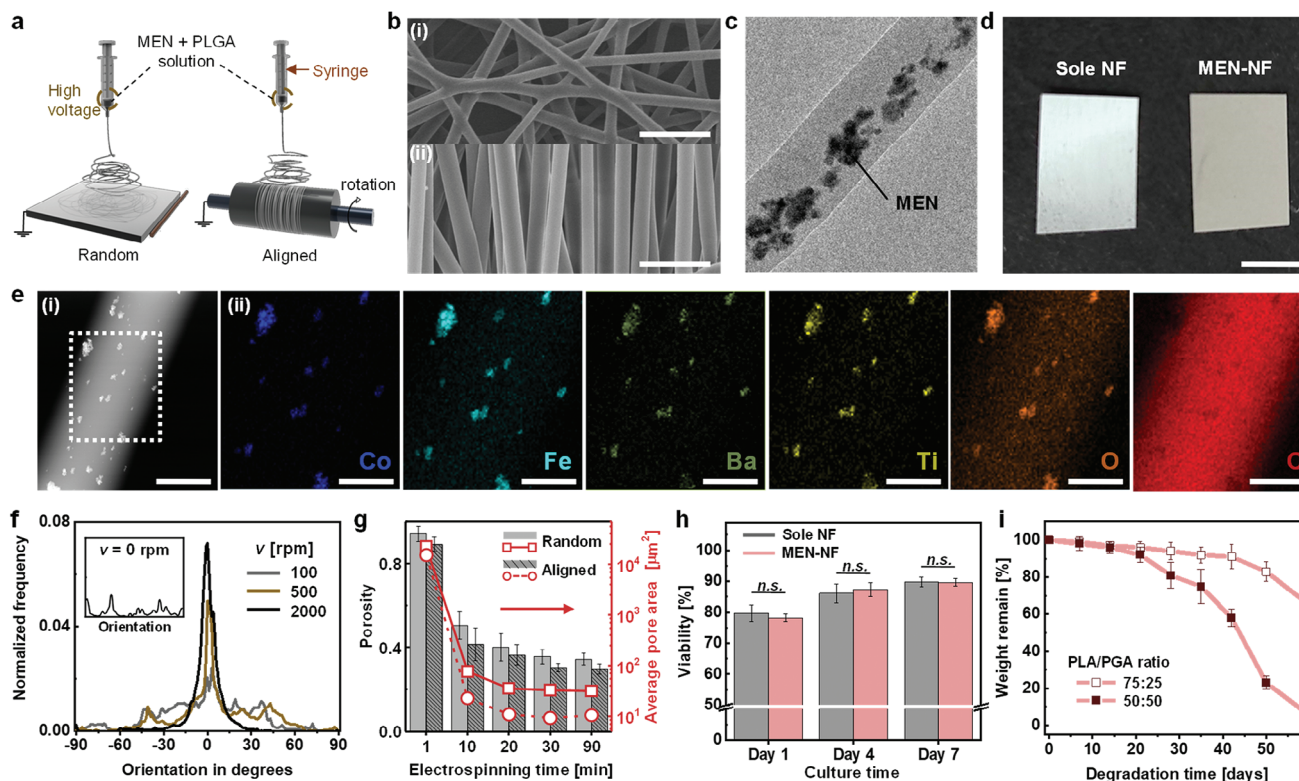


Figure 3. Fabrication and characterization of MEN-NF bioelectronic paper. a) Schematic diagram of the MEN-NF fabrication using electrospinning system. Random and aligned orientation of MEN-NF is achieved using plate and rotating drum collector, respectively. b) SEM images of MEN-NF with i) random and ii) aligned microstructure (scale bars, 3 μm). c) TEM image (bright field) of MEN-NF (scale bar, 200 nm). d) Comparison photograph of fabricated MEN-NF and sole NF without MEN integration (scale bar, 1 cm). e) i) TEM image of MEN-NF (scale bar, 1 μm) and ii) EDS mapping images corresponding to the area of the white dotted box (scale bars, 500 nm). f) Orientation distribution analysis results for different rotating speed ν using a drum collector. Inset: orientation distribution using a plate collector. g) Porosity (left y-axis) and average pore area (right y-axis) of random and aligned MEN-NF as a function of electrospinning time. h) PC12 viability over 7 days of culturing on sole NF and MEN-NF (n.s., not significant). i) Weight remains of MEN-NF with different PLA/PGA ratios as a function of degradation time in PBS at 37.5 $^{\circ}\text{C}$.

distributed MENs within the NF template (Figure 3d). In addition, EDS results in Figure 3e revealed that the MENs loaded into the polymeric NF were indeed as-prepared CFO@BTO nanoparticles, with all their constituent elements detected within the NF carbon element matrix.

Next, the microstructural tunability including alignment degree and porosity was quantitatively investigated under different electrospinning conditions from SEM images (see Figure S4, Supporting Information, for the representative images). Controlling the alignment of nanofibers as scaffolds for tissue engineering applications can provide a substantial control over various cellular activities.^[43,44] As shown in Figure 3f, the degree of MEN-NF alignment increased as the drum rotation speed increased, with fewer and higher peaks in the MEN-NF orientation angle distribution. The best alignment was achieved at a rotation speed of 2000 rpm, and MEN-NF was difficult to collect at a higher speed due to the high air turbulence generated by the drum rotation.

The average pore size of the electrospun MEN-NF is another considerable factor with respect to diffusion permeability. As shown in Figure 3g, the porosity initially decreased dramatically and then began to converge when the electrospinning time reached 20 min. Furthermore, since aligned fibers have a more organized structure that increases packing density, the random

MEN-NF had higher porosity and average pore area than aligned MEN-NF, which could possibly allow for more efficient nutrient and waste exchange^[45] in electrical stimulation-dominant applications.

In addition to the biocompatibility evaluation in MEN-dispersed culture media, cell viability and proliferation rate of PC12 were further investigated on MEN-NF at multiple time points. As shown by the in vitro cytotoxicity test results in Figure 3h, the relative cell viability for both sole NF and MEN-NF similarly increased over time as they gradually proliferated without appreciable toxic effects and showed >89% viability on day 7 (see Figure S5a, Supporting Information, for live/dead assay fluorescent images). The proliferation rate, assessed through 3-(4,5-dimethylthiazol-2-yl)-2,5-diphenyltetrazolium bromide (MTT) analysis, exceeded 200% on day 7 for both conditions (Figure S5b, Supporting Information). Although the proliferation rate on MEN-NF slightly decreased over time compared to that on the sole NF, the overall proliferation trend closely resembled one another. Taken together, the incorporation of MEN into NF made no discernible difference in the metabolism related to cell survival and proliferation.

Another merit of using the PLGA NF template is the ability to control the rate of biodegradation. Since PLGA is a copolymer

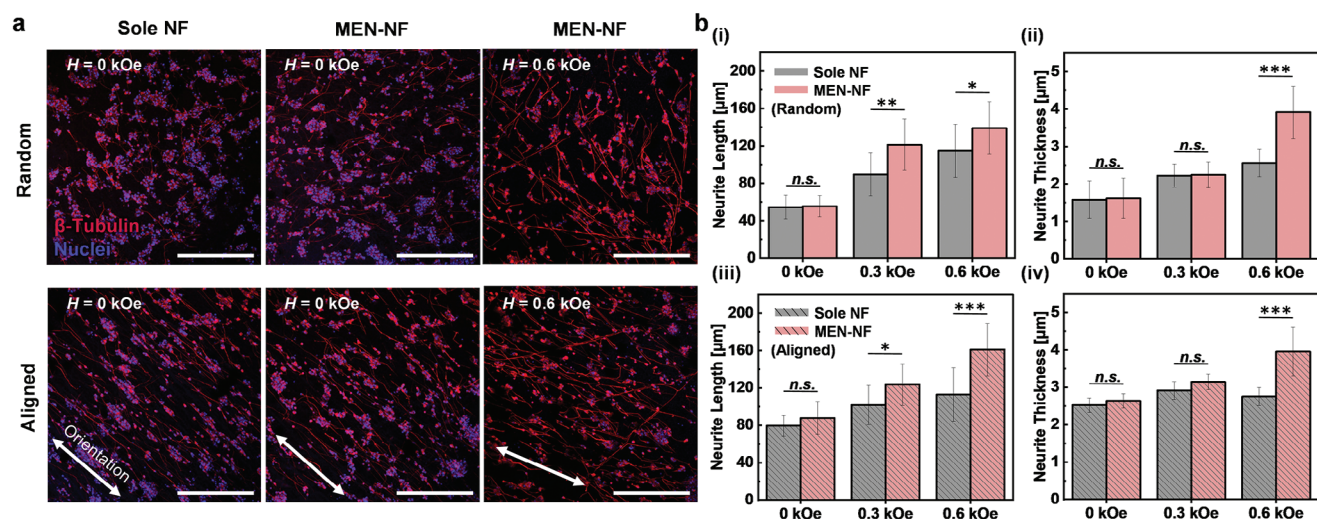


Figure 4. Neuronal differentiation of PC12 according to alignment, magnetic stimulation, and presence of MEN into NF. a) Fluorescence images of β -tubulin (red) and nuclei (blue) stained PC12 after 7 days of culture on sole NF and MEN-NF with different fiber orientation and external magnetic field intensity (scale bars, 200 μ m; see Figure S6, Supporting Information, for complete set of images with various parameters). b) neurite length and neurite thickness of PC12 on i,ii) random and iii,iv) aligned sole NF and MEN NF according to applied magnetic field intensity (n.s., not significant, $*P < 0.05$, $**P < 0.01$, and $***P < 0.001$).

of polylactic acid (PLA) and polyglycolic acid (PGA), a higher proportion of PGA leads to a faster rate of degradation.^[46] To assess the biodegradability of the MEN-NF, the as-prepared MEN-NFs with different PLGA contents were submerged in PBS at 37.5 °C for a duration of 60 days, and the remaining weight was recorded. As shown in Figure 3i, the PLGA with a 50:50 ratio of PLA/PGA exhibited faster biodegradation than a 75:25 ratio. In both cases, the weight losses were initially small but then suddenly increased significantly. This characteristic could potentially be advantageous in clinical scenarios with minimal functional loss for treatments during the non-stop biodegradation process.

2.3. In Vitro Demonstrations of the MEN-NF Bioelectronic Paper

To evaluate the capability of MEN-NF to regulate cell morphology and perform wireless electrical stimulation, PC12 cells were grown and differentiated on sole NF, MEN-NF with random and aligned orientations. PC12 cells were chosen as they have been widely used to study the effects of electrical stimulation on neuronal cells due to their neuron-like behaviors upon differentiation. PC12 cells are embryonic neuroblasts that grow in clusters, but as they differentiate, they undergo neurite outgrowth, which can be accelerated when exposed to electrical stimulation.^[47] Then, an external DC magnetic field was applied 2 h per day with intensities of 0, 0.3, and 0.6 kOe, which is up to near where the maximum α_{ME} was achieved (Figure 2e). The calculated voltage $V = \int t \times \alpha_{ME} dH$ corresponding to each magnetic field intensity was $V \approx 0$, ≈ 65.3 , and ≈ 145.5 mV, respectively.

First, The PC12 cells were treated with a differentiation medium when seeded on sole NF or MEN-NF. After 7 days of culture, we fluorescently labeled the β -tubulin, which is a hallmark of neuron cells associated with the growth of specific neuronal cell extensions called axons and dendrites.^[48] Staining β -tubulin can allow us to identify and quantify neurite outgrowth, and is

widely employed to determine the degree of neuronal differentiation and functional regeneration.^[48] In Figure 4a, the representative fluorescent images of the PC12 cells clearly showed that aligned NFs can guide the orientation of neurite outgrowth regardless of the presence of MEN. The neurite outgrowth of PC12 cells was quantified by evaluating the neurite length and neurite thickness from fluorescent images (Figure S6, Supporting Information). Regardless of the orientation of the NF, the incorporation of MEN increased both neurite length and thickness under an external magnetic field, which was notably pronounced at the field intensity of 0.6 kOe (Figure 4b). This enhancement is possibly due to the regulation of the voltage-gated Ca^{2+} channels by the transduced electric field, which ultimately affects the expression of neurogenic proteins and enhances the neural functional expression of the PC12 cells. In detail, electrical stimulation can change extracellular Ca^{2+} concentration, resulting in an influx of Ca^{2+} that changes transmembrane potential and leads to depolarization.^[49,50] This Ca^{2+} change and influx could activate Ca^{2+} /calmodulin-dependent protein kinase to promote neurite development.^[51] Overall, these results suggest that MEN-NF can wirelessly deliver electrical stimulation, which contributes to the neurofunctional phenotype maturation for PC12 cells.

We note that applying the external magnetic field also increased neurite length and thickness even on sole NF, but to a lesser extent than on MEN-NF (Figure 4b). This enhancement can be attributed to the hindrance of cell aggregation by the magnetic field, which increases the differentiation efficiency of the PC12 cells. In the absence of a magnetic field, the PC12 cells preferentially migrated and formed cell clusters even in the presence of biochemical stimulations such as low serum concentration and NGF (Figure S7a(i), Supporting Information). The cells within a cluster were less in favor of bearing neurites during differentiation, with only a few short and thin neurites observed (Figure S7a(ii), Supporting Information), possibly because PC12 aggregation can sequester membrane proteins such as β -catenin

and restrict its availability for biochemical signaling to the nucleus at the early stage of neural differentiation.^[52] However, as the intensity of the applied magnetic field increased, the average PC12 cell cluster size decreased (Figure S7b,d, Supporting Information). This effect can be ascribed to the reorientation of membrane phospholipids during magnetic field exposure, which leads to the deformation of embedded ion channels and consequent alteration of their activation kinetics.^[53,54] As a result, PC12 cells were distributed more evenly with increasing magnetic field intensity (Figure S6, Supporting Information), leading to an increase in the percentage of neurite-bearing cells during differentiation (Figure S7c,e, Supporting Information). Nonetheless, the magnetic field effect was more pronounced and significant in MEN-NF, suggesting the beneficial impact of magnetoelectric functionality on neuronal differentiation.

To further reveal the effects of stimulation time on cell behaviors, we compared the effects of applying stimulation for 2 h per day against 6 h per day on PC12 cells cultured in growth media (Figure S8, Supporting Information) and differentiation media (Figure S9, Supporting Information) over 7 days. As the length of exposure to the magnetic field increased, the size of the cell cluster decreased (Figure S8a,b, Supporting Information). This outcome aligned with the trend where an increase in magnetic field intensity leads to a reduction in cell cluster size (Figure S7, Supporting Information). Also, an overabundance of magnetic field exposure (6 h per day) was found to have a negative impact on cell growth and differentiation, leading to decreased viability (Figure S8c, Supporting Information) and neurite length (Figure S9c, Supporting Information). This outcome may be attributed to the activation of nitric oxide synthesis via Ca^{2+} /calmodulin stimulation and consequent oxidative stress.^[49] Likewise, in MEN-NF settings with excessive electrical stimulation conditions (6 h per day), both growth and differentiation of PC12 showed unfavorable outcomes with low viability (Figure S8c, Supporting Information) and low neurite length (Figure S9c, Supporting Information). One possible mechanism suggests that reactive oxygen species (ROS) such as superoxide anions (O_2^-) and hydrogen peroxide (H_2O_2) are generated within cells under electrical stimulation. Therefore, intense or prolonged electrical stimulation can result in an excessive generation of intracellular ROS, which can induce cell apoptosis and inhibit cellular activities.^[47,55] These findings align with previous studies that primarily utilize stimulation periods of less than 2 h per day,^[47,56] suggesting that deviations from the optimal duration and intensity of electrical stimulation could result in adverse effects on both cell proliferation and differentiation.^[57]

2.4. Macrostructure Programmability of the Bioelectronic Paper

We next demonstrate the macrostructural programmability of the MEN-NF bioelectronic paper. First, the electrospun MEN-NF was collected for 15 min to obtain a free-standing bioelectronic paper with handleable thickness ($\approx 50 \mu\text{m}$). Then, the bioelectronic paper can be cut into arbitrary shapes and scales while retaining its function and microstructure as illustrated in Figure 5a, and the macrostructure can be further customized using simple methods such as rolling, cutting, inward folding, and outward folding. For example, preparing rectangular bioelectronic paper

with different scales, followed by rolling with a carbon rod of varying diameters can yield conduit structures with various diameters (Figure 5b) or lengths (Figure 5c). Notably, the exceptional flexibility of our bioelectronic paper is clearly evident in the rolled paper depicted in Figure 5b, with a demonstrated bending radius of $400 \mu\text{m}$. Also, the bioelectronic paper can be folded using origami folding techniques such as layered folding to create miura-ori (Figure 5d) and reverse folding to create waterbomb base macrostructure (Figure 5e). Furthermore, the bioelectronic paper can be subjected to kirigami cutting technique and elastically stretched to create out-of-plane buckled structure (Figure 5f) or origami-kirigami combined techniques to create a pop-up structure (Figure 5g). Last, we show that bioelectronic paper, due to its flexibility, could be used simply in 2D planar shape to conform to complex surfaces with combined positive and negative Gaussian curves (Figure 5h). We note that a single electrospun bioelectronic paper (with approximate area of 225 cm^2) could mass-fabricate various personalized bioelectronic implants, as it could be cut into hundreds of $0.5 \text{ cm} \times 1.5 \text{ cm}$ sheets, for example, to create conduits in Figure 5b (right side) or more than a hundred of $1 \text{ cm} \times 2 \text{ cm}$ sheets to create other macrostructure using different tailoring method as shown in Figure 5f.

To show that the bioelectronic paper can retain its structural integrity and support cell adhesion during reconstruction to a 3D structure, PC12 cells were differentiated and electrically stimulated on the bioelectronic paper with aligned orientation for 7 days, and then the bioelectronic paper was folded to a pyramid macrostructure (Figure 5i). The 3D topological image captured at the peak of the pyramid macrostructure clearly showed the intricate controllability of the bioelectronic paper over local height variations during the 3D structuring process (Figure 5j). The PC12 cells were densely populated and well-distributed on this 3D structure, with no noticeable cell detachment (Figure 5k). Also, the neurites of the PC12 cells were well aligned, even in the vicinity of the mountain crease where there is an abrupt change in local height (Figure 5l). These findings suggest the structure of the bioelectronic paper remains intact throughout the 3D reconstruction process, underscoring the structural stability and suitability of the bioelectronic paper for 3D applications.

3. Conclusion

This work presents a promising strategy for the development of flexible and biodegradable wireless bioelectronic implants that can be simply customized for various clinical and physical circumstances. The combination of nanoscale magnetoelectric and biodegradable fibrous materials offers advantages over traditional system-level wireless electronic devices that rely on intricate assembly of bulky components that cannot be redesigned post-fabrication.

We have shown that we can remotely generate electric polarization of the MEN with an external magnetic field. The MEN was lead-free and did not exhibit a cytotoxic response. Also, by distributing MENs into biodegradable PLGA NF, i) overdosing of MENs can be avoided, achieving high biocompatibility and localized electrical stimulation to target, ii) the NF with flexibility, high surface-to-volume ratio, and porous structure can provide biomimetic environment that resembles native ECM, iii) microstructure of the NF can be tuned to control cell response or

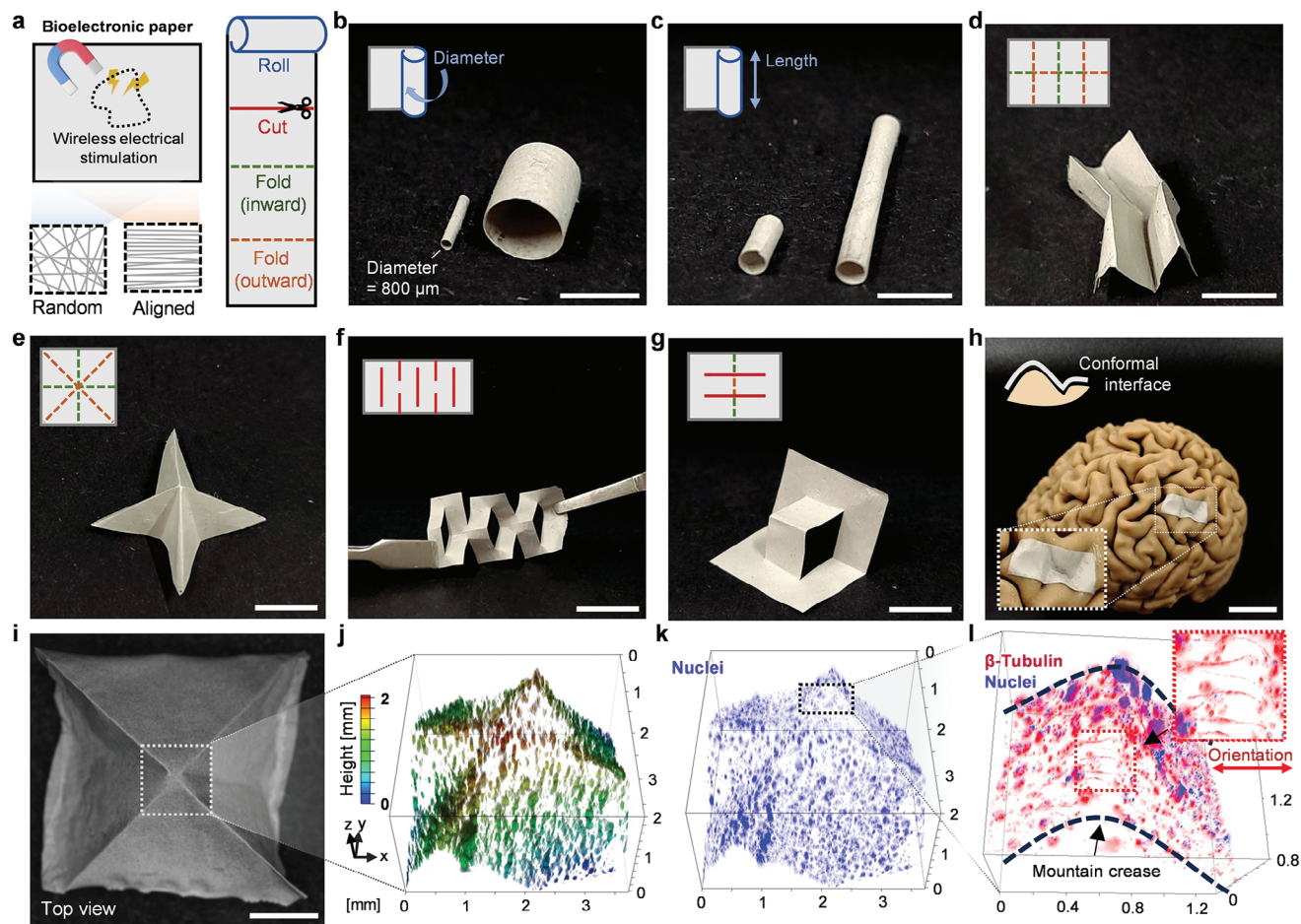


Figure 5. Macrostructure programming of MEN-NF bioelectronic paper. a) Schematic illustration of bioelectronic paper retaining functionality and microstructure under rolling, cutting, and folding. b,c) photographs of conduit macrostructures with various diameters and lengths, rolled from rectangular sheets with different scales (scale bars, 5 mm). d,e) Miura-ori and waterbomb base macrostructures, tailored using origami folding techniques (scale bars, 1 cm). f) out-of-plane buckled macrostructure under in-plane tensile strain, tailored using kirigami cutting technique (scale bar, 1 cm). g) Pop-up macrostructure, tailored using origami-kirigami combinative method (scale bar, 1 cm). h) 2D planar sheet of bioelectronic paper conforming to a complex surface (scale bar, 2 cm). i) Stereo microscopy image of a pyramid macrostructure (scale bar, 3 mm). j) 3D topographic map at the peak of the pyramid macrostructure shown in (i), indicated by white dotted box. The color bar indicates local height variations. k) Fluorescence 3D image of PC12 cells on pyramid macrostructure. The nuclei of PC12 are stained and shown in blue. l) Fluorescence 3D image of the β -tubulin (red) and nuclei (blue) stained PC12, enlarged view of the black dotted box in (k). The inset shows enlarged view of the PC12 at the mountain crease (red dotted box).

diffusion permeability, iv) the NF, which constitute the majority of the MEN-NF (≈ 0.16 g of MEN per 1 mL of PLGA), can be biodegraded with controllable biodegradation speed using PLGA with different PGA and PLA ratios. Furthermore, we have demonstrated evidence that this combined bioelectronic paper can affect cell orientations and wirelessly modulate neuronal cell activity in vitro with a mild external magnetic field (0.6 kOe). Finally, our bioelectronic paper with an advantageously low area density of 0.03 g cm^{-2} can mass-produce a variety of 3D macrostructures using simple origami and kirigami techniques, or specifically shaped 2D structures that can conform to complex surfaces.

The results herein demonstrate the potential of combining nanoscale MEN and biodegradable NF for the simple and rapid personalization of wireless bioelectronic implants, which could facilitate the clinical management of various disorders. In the future, it will be important to optimize structures and stimulation conditions for targeted applications, along with the evalua-

tion of wireless stimulation efficacy and long-term biosafety in animal disease models. The bioelectronic paper, in principle, can be simply customized to organ-scales of several tens of centimeters or miniaturized to sub-micrometer scales for minimally invasive operations, as the magnetolectricity or microstructure does not depend on its scale. Also, the biodegradable bioelectronic paper could eliminate the need for secondary removal surgery post-implantation, and the biodegradation rate can be further adjusted according to the targeted treatment period to reduce long-term risks. Overall, our bioelectronic paper with facile and broad applicability, could open up a new scheme toward minimally invasive, and biodegradable wireless bioelectronic implants.

4. Experimental Section

Materials: For MEN synthesis, cobalt(II) nitrate hexahydrate ($\text{Co}(\text{NO}_3)_2 \cdot 6\text{H}_2\text{O}$, 99.999% trace metals basis), iron(III) nitrate

nonahydrate (Fe(NO₃)₃·9H₂O, ACS reagent, ≥98%), polyvinylpyrrolidone (average mol. wt. 40 000), sodium borohydride (NaBH₄, powder, ≥98.0%), barium carbonate (BaCO₃, 99.999% trace metals basis), citric acid (ACS reagent, ≥99.5%), and titanium (IV) isopropoxide (Ti₄(OCH₃)₁₆, ≥97.0%) were purchased from Sigma-Aldrich, and all materials were used without further purification.

For electrospinning, PLGA (PLA:PGA = 50:50, 75:25), 1,1,1,3,3,3-hexafluoro-2-propanol, and gelatin (300 bloom, type A) were purchased from Sigma-Aldrich.

For cell culture, RPMI1640, opti-MEM, horse serum (HS), fetal bovine serum (FBS), and penicillin–streptomycin (PS) were purchased from Thermo Fisher Scientific and NGF was purchased from Sigma-Aldrich.

For in vitro analysis, MTT, anti-tubulin-βIII antibody, 4',6-diamidino-2-phenylindole (DAPI) were purchased from Sigma-Aldrich and donkey anti-rabbit Alex Fluor™ 647, LIVE/DEAD Viability/Cytotoxicity Kit were purchased from Thermo Fisher Scientific.

Synthesis of CFO Nanoparticles: CFO nanoparticles and CFO@BTO core–shell MENs were prepared in accordance with standard procedure^[58] with minor modifications.

To prepare CFO nanoparticles, cobalt (II) nitrate hexahydrate (0.058 g) and iron (III) nitrate nonahydrate (0.16 g) were dissolved in aqueous solution (15 mL) under stirring. Next, a different aqueous solution (5 mL) containing sodium borohydride (0.9 g) and polyvinylpyrrolidone (0.2 g) was added to the mixture, then hydrothermal treatment was applied with a stainless-steel autoclave at 120 °C for 12 h. The resulting precipitates were washed with deionized water three times, magnetically collected using a neodymium magnet, and finally dried in a vacuum oven at 80 °C for 12 h.

Synthesis of CFO@BTO Core/Shell MENs: To prepare CFO@BTO core–shell MENs, barium carbonate (0.029 g) was dissolved in aqueous solution (30 mL) containing citric acid (0.1 g). Next, a different ethanolic solution (30 mL) containing titanium (IV) isopropoxide (0.048 mL) and citric acid (1 g) was added to the mixture. Then, as-prepared CFO nanoparticles (0.1 g) were sonicated in deionized water (10 mL) for 30 min, added to the mixture, and sonicated for an additional 2 h. This solution was then dried on a hot plate at 100 °C for 12 h, calcined in a box furnace at 650 °C for 3 h, and then ground with a mortar and pestle.

Morphology, Constituent Element, and Crystal Structure Analysis of CFO and CFO@BTO: The morphologies of CFO nanoparticles and CFO@BTO core–shell MENs were analyzed using SEM (S-4800, Hitachi) and TEM (JEM-2100, JEOL), with the acceleration voltage of 10 and 200 kV, respectively. The elemental mapping images were acquired using an energy-dispersive X-ray spectrometer integrated with the JEM-2100 instrument. The relative ratios of the elemental contents were determined using ICP-OES (700-ES, Varian). The crystal structures were characterized by an X-ray diffractometer (AXS D8 ADVANCE, Bruker) in the 2θ range of 10–80° with Cu Kα radiation (λ = 1.5406 Å). The diffraction peaks were identified using the crystallography open database (COD).

Magnetolectric Coefficient Characterization: The Magnetolectric coefficient was measured according to previous lock-in techniques.^[37] To prepare the sample, The powder MENs were pressed into a pellet of 5 mm × 1 mm (diameter × thickness) at a pressure of 60 MPa in a hydraulic press. Next, the pellet was pasted with Ag paste as electrodes and corona-poled (14 kV, 0.01 mA). Then, an AC magnetic field (generated by a Helmholtz coil) of amplitude 1 Oe, which was superimposed on a DC magnetic field (generated by an electromagnet) of up to 2 kOe was applied to the sample. The voltage from the specimen was recorded at room temperature using the measurement system including a lock-in amplifier (SR850, Stanford Research System), a bipolar amplifier (BA4825, NF Corporation), and a DC current amplifier (BOP 36-12ML, KEPCO). The magnetolectric coefficient α_{ME} was calculated using the equation as follows

$$\alpha_{ME} = \left(\frac{\delta E}{\delta H} \right) = \frac{1}{t} \left(\frac{\delta V}{\delta H} \right) \quad (1)$$

where V is the voltage and t is the thickness of the sample.

Preparation of MEN-NF Bioelectronic Paper: To prepare the MEN-PLGA solution, 20 mg of MENs were dispersed in 1 mL of 1 wt% gelatin

solution dissolved in 1,1,1,3,3,3-hexafluoro-2-propanol solvent using a probe sonication (VCX 750, Sonics and Materials) at 750 W, 20 kHz, the amplitude of 50%, and a total running time of 30 min with sonication interval of 5/5 s ON/OFF. Gelatin was incorporated as previous findings had shown that it can enhance neuronal adhesion and differentiation compared to using synthetic nanofibrous scaffolds alone.^[59] The solution was kept in an ice bath during sonication to avoid overheating. Then PLGA was dissolved into the mixture (15 wt%) and sonicated for another 10 min.

This solution was then used to fabricate MEN-nanofibers using an electrospinning instrument (eS-robot, Nano NC). The MEN-PLGA solution was loaded into a syringe connected to a 25 G metal capillary and supplied at a feeding rate of 0.6 mL h⁻¹ with the capillary-to-collector distance kept constant at 13 cm. Then, a voltage was connected to the end of a capillary containing the solution and a collector, and gradually increased up to 14 kV. A plate collector was used to collect random nanofibers and a rotating drum collector (diameter of 10 cm) was used to collect aligned nanofibers. Under a mild increase in voltage, the hemispherical surface of the solution at the end of the capillary was polarized and extended by the electric field, creating a Taylor cone. By increasing the electric field further, the critical value at which the repulsive electrostatic force overcomes the surface tension was reached, and the charged strand was squirted out from the Taylor cone. The strand of solution underwent a process of instability and stretching, during which the solvent evaporates. Electrospun MEN-NF was placed under a vacuum oven at 50 °C for 12 h for further evaporation of the solvent.

Characterization of MEN-NF Bioelectronic Paper: The morphologies of MEN-NF were acquired with SEM (S-4800, Hitachi) and TEM (JEM-2100, JEOL). Elemental mapping images were obtained using an energy-dispersive X-ray spectrometer integrated JEM-2100 instrument. The diameter, degree of alignment, porosity, and average pore area of MEN-NF were analyzed using ImageJ software.

Cell Preparation and Culture: PC12 cells were obtained from the Korean Cell Line Bank (Seoul, Korea). PC12 cells were grown in RPMI 1640 supplemented with 10% HS, 5% FBS, and 1% PS. PC12 cells underwent neuronal differentiation in Opti-MEM supplemented with 50 ng mL⁻¹ of NGF, 0.5% FBS, and 1% PS. Cell growth and differentiation progressed under 37 °C, 5% CO₂ conditions, and the media was replaced every other day.

In Vitro Evaluations: The viability of PC12 on both culture flasks and the NF matrix was measured by counting live and dead cells at specific time points. After PBS washing, the cells were treated with calcein-AM (green) and ethidium homodimer-1 (red) to label fluorescence into live and dead cells, respectively. In addition, an MTT assay was performed for quantitative proliferation rate measurement. Fresh growth media supplemented with 0.5 mg mL⁻¹ of MTT was replaced and incubated for 4 h. The amount of reduced MTT reagent by living cell metabolism was measured by the absorbance at 570 nm.

To apply the external magnetic field, four well plates containing PC12 cells on sole NF or MEN-NF were fixed at specific surface points of a permanent magnet for 2 h per day for 7 days. The field intensities of the permanent magnet were measured with a Gauss meter at the specified locations.

Differentiated PC12 cells were visualized through immunofluorescent labeling with tubulin-βIII, a hallmark of neuronal differentiation. The samples were fixed with 4% paraformaldehyde for 10 min, permeabilized with 0.1% Triton-X 100 for 30 min, and blocked with 1% bovine serum albumin and 0.1% sodium azide for 2 h. The samples were treated with diluted anti-tubulin-βIII antibody (1:500) overnight at 4 °C, followed by incubation in diluted secondary antibody with Alex Fluor 647 (1:1000) for 1 h at room temperature. Finally, nuclei were stained with DAPI for 15 min. The samples were washed three times with PBS in between each step and were imaged by confocal microscopy (FV 1000, Olympus). For the 3D structure, the optical top-view image was taken by a stereo microscope (Axio Zoom, ZEISS), and the fluorescence images were taken by a wide-field fluorescence microscope (TUNDER, Lecia). To measure differentiation efficiency, cluster size, neurite length, and thickness, cellular morphology from microscopic cell images was characterized through ImageJ software.

Statistical Data Analysis: All statistical measurements were performed by Origin and Excel. All data were shown as mean \pm standard deviation (SD). Statistical significance was assessed using Student's *t*-test or one way ANOVA followed by Turkey's post hoc test between different samples. Significance levels were determined by (*) $P < 0.05$, (**) $P < 0.01$, and (***) $P < 0.001$.

Supporting Information

Supporting Information is available from the Wiley Online Library or from the author.

Acknowledgements

J.K.C., S.K., and A.L. contributed equally to this work. This work was supported by the National Research Foundation (NRF; RS-2023-00302525, NRF-2022R1A2C2009174, NRF-2020R1A2C2102842, NRF-2021R1A4A3033149, and the NRF-2019 Global Ph.D. Fellowship Program), Korea Institute for Advancement of Technology (KIAT; P0023703, HRD Program for Industrial Innovation) grants funded by the Korean government, and the Fundamental Research Program of the Korea Institute of Material Science (PNK7630).

Conflict of Interest

The authors declare no conflict of interest.

Data Availability Statement

The data that support the findings of this study are available from the corresponding author upon reasonable request.

Keywords

biodegradable, bioelectronic implant, magnetoelectric nanoparticle, nanofiber, personalization, wireless stimulation

Received: October 24, 2023
Revised: December 20, 2023
Published online:

- [1] L. Peeples, *Proc. Natl. Acad. Sci. USA* **2019**, *116*, 24379.
- [2] C. Chen, X. Bai, Y. Ding, I.-S. Lee, *Biomater. Res.* **2019**, *23*, 25.
- [3] S. Javeed, A. H. Faraji, C. Dy, W. Z. Ray, M. R. MacEwan, *Interdiscip. Neurosurg.* **2021**, *24*, 101117.
- [4] M. Griffin, A. Bayat, *Eplasty* **2011**, *11*, e34.
- [5] A. L. Waldo, J. L. Wells, T. B. Cooper, W. A. H. Maclean, *Prog. Cardiovasc. Dis.* **1981**, *23*, 451.
- [6] D. M. Thompson, A. N. Koppes, J. G. Hardy, C. E. Schmidt, *Annu. Rev. Biomed. Eng.* **2014**, *16*, 397.
- [7] A. L. Benabid, *Curr. Opin. Neurobiol.* **2003**, *13*, 696.
- [8] Y. Luo, Y. Sun, X. Tian, X. Zheng, X. Wang, W. Li, X. Wu, B. Shu, W. Hou, *Front. Aging Neurosci.* **2021**, *13*, 619543.
- [9] L. R. Hochberg, D. Bacher, B. Jarosiewicz, N. Y. Masse, J. D. Simeral, J. Vogel, S. Haddadin, J. Liu, S. S. Cash, P. Van Der Smagt, J. P. Donoghue, *Nature* **2012**, *485*, 372.
- [10] J. Rivnay, H. Wang, L. Fenno, K. Deisseroth, G. G. Malliaras, *Sci. Adv.* **2017**, *3*, e1601649.
- [11] Y. Liu, J. Liu, S. Chen, T. Lei, Y. Kim, S. Niu, H. Wang, X. Wang, A. M. Foudeh, J. B.-H. Tok, Z. Bao, *Nat. Biomed. Eng.* **2019**, *3*, 58.
- [12] Y. S. Choi, Y.-Y. Hsueh, J. Koo, Q. Yang, R. Avila, B. Hu, Z. Xie, G. Lee, Z. Ning, C. Liu, Y. Xu, Y. J. Lee, W. Zhao, J. Fang, Y. Deng, S. M. Lee, A. Vázquez-Guardado, I. Stepien, Y. Yan, J. W. Song, C. Haney, Y. S. Oh, W. Liu, H.-J. Yoon, A. Banks, M. R. Macewan, G. A. Ameer, W. Z. Ray, Y. Huang, T. Xie, et al., *Nat. Commun.* **2020**, *11*, 5990.
- [13] Y. S. Choi, R. T. Yin, A. Pfenniger, J. Koo, R. Avila, K. B. Lee, S. W. Chen, G. Lee, G. Li, Y. Qiao, A. Murillo-Berlioz, A. Kiss, S. Han, S. M. Lee, C. Li, Z. Xie, Y.-Y. Chen, A. Burrell, B. Geist, H. Jeong, J. Kim, H.-J. Yoon, A. Banks, S.-K. Kang, Z. J. Zhang, C. R. Haney, A. V. Sahakian, D. Johnson, T. Efimova, et al., *Nat. Biotechnol.* **2021**, *39*, 1228.
- [14] Y. S. Choi, H. Jeong, R. T. Yin, R. Avila, A. Pfenniger, J. Yoo, J. Y. Lee, A. Tzavelis, Y. J. Lee, S. W. Chen, H. S. Knight, S. Kim, H.-Y. Ahn, G. Wickerson, A. Vázquez-Guardado, E. Higbee-Dempsey, B. A. Russo, M. A. Napolitano, T. J. Holleran, L. A. Razzak, A. N. Miniovich, G. Lee, B. Geist, B. Kim, S. Han, J. A. Brennan, K. Aras, S. S. Kwak, J. Kim, E. A. Waters, et al., *Science* **2022**, *376*, 1006.
- [15] G. Lee, E. Ray, H.-J. Yoon, S. Genovese, Y. S. Choi, M.-K. Lee, S. Sahin, Y. Yan, H.-Y. Ahn, A. J. Bandodkar, J. Kim, M. Park, H. Ryu, S. S. Kwak, Y. H. Jung, A. Odabas, U. Khandpur, W. Z. Ray, M. R. Macewan, J. A. Rogers, *Sci. Adv.* **2022**, *8*, eabp9169.
- [16] D. Afanasenkau, D. Kalinina, V. Lyakhovetskii, C. Tondera, O. Gorsky, S. Moosavi, N. Pavlova, N. Merkulyeva, A. V. Kalueff, I. R. Mineev, P. Musienko, *Nat. Biomed. Eng.* **2020**, *4*, 1010.
- [17] S.-W. Hwang, H. Tao, D.-H. Kim, H. Cheng, J.-K. Song, E. Rill, M. A. Brenckle, B. Panilaitis, S. M. Won, Y.-S. Kim, Y. M. Song, K. J. Yu, A. Ameen, R. Li, Y. Su, M. Yang, D. L. Kaplan, M. R. Zakin, M. J. Slepian, Y. Huang, F. G. Omenetto, J. A. Rogers, *Science* **2012**, *337*, 1640.
- [18] J. Koo, M. R. Macewan, S.-K. Kang, S. M. Won, M. Stephen, P. Gamble, Z. Xie, Y. Yan, Y.-Y. Chen, J. Shin, N. Birenbaum, S. Chung, S. B. Kim, J. Khalifeh, D. V. Harburg, K. Bean, M. Paskett, J. Kim, Z. S. Zohny, S. M. Lee, R. Zhang, K. Luo, B. Ji, A. Banks, H. M. Lee, Y. Huang, W. Z. Ray, J. A. Rogers, *Nat. Med.* **2018**, *24*, 1830.
- [19] D. K. Piech, B. C. Johnson, K. Shen, M. M. Ghanbari, K. Y. Li, R. M. Neely, J. E. Kay, J. M. Carmena, M. M. Maharbiz, R. Muller, *Nat. Biomed. Eng.* **2020**, *4*, 207.
- [20] Y. Jiang, A. A. Trotsyuk, S. Niu, D. Henn, K. Chen, C.-C. Shih, M. R. Larson, A. M. Mermin-Bunnell, S. Mittal, J.-C. Lai, A. Saberi, E. Beard, S. Jing, D. Zhong, S. R. Steele, K. Sun, T. Jain, E. Zhao, C. R. Neimeth, W. G. Viana, J. Tang, D. Sivaraj, J. Padmanabhan, M. Rodrigues, D. P. Perrault, A. Chattopadhyay, Z. N. Maan, M. C. Leeolou, C. A. Bonham, S. H. Kwon, et al., *Nat. Biotechnol.* **2023**, *41*, 652.
- [21] J. C. Chen, P. Kan, Z. Yu, F. Alrashdan, R. Garcia, A. Singer, C. S. E. Lai, B. Avants, S. Crosby, Z. Li, B. Wang, M. M. Felicella, A. Robledo, A. V. Peterchev, S. M. Goetz, J. D. Hartgerink, S. A. Sheth, K. Yang, J. T. Robinson, *Nat. Biomed. Eng.* **2022**, *6*, 706.
- [22] A. Singer, S. Dutta, E. Lewis, Z. Chen, J. C. Chen, N. Verma, B. Avants, A. K. Feldman, J. O'malley, M. Beierlein, C. Kemere, J. T. Robinson, *Neuron* **2020**, *107*, 631.
- [23] J. Koo, S. B. Kim, Y. S. Choi, Z. Xie, A. J. Bandodkar, J. Khalifeh, Y. Yan, H. Kim, M. K. Pezhouh, K. Doty, G. Lee, Y.-Y. Chen, S. M. Lee, D. D'andrea, K. Jung, K. Lee, K. Li, S. Jo, H. Wang, J.-H. Kim, J. Kim, S.-G. Choi, W. J. Jang, Y. S. Oh, I. Park, S. S. Kwak, J.-H. Park, D. Hong, X. Feng, C.-H. Lee, et al., *Sci. Adv.* **2020**, *6*, eabb1093.
- [24] P. Gutruf, R. T. Yin, K. B. Lee, J. Ausra, J. A. Brennan, Y. Qiao, Z. Xie, R. Peralta, O. Talarico, A. Murillo, S. W. Chen, J. P. Leshock, C. R. Haney, E. A. Waters, C. Zhang, H. Luan, Y. Huang, G. Trachiotis, I. R. Efimov, J. A. Rogers, *Nat. Commun.* **2019**, *10*, 5742.
- [25] S. Kopyl, R. Surmenev, M. Surmeneva, Y. Fetisov, A. Kholkin, *Mater. Today Bio* **2021**, *12*, 100149.
- [26] Z. Yu, J. C. Chen, F. T. Alrashdan, B. W. Avants, Y. He, A. Singer, J. T. Robinson, K. Yang, *IEEE Trans Biomed. Circuits Syst.* **2020**, *14*, 1241.

- [27] E. H. Apu, M. Nafujjaman, S. Sandeep, A. V. Makela, A. Khaleghi, S. Vainio, C. H. Contag, J. Li, I. Balasingham, T. Kim, N. Ashammakhi, *Mater. Chem. Front.* **2022**, *6*, 1368.
- [28] A. Kaushik, R. D. Jayant, R. Nikkhah-Moshaie, V. Bhardwaj, U. Roy, Z. Huang, A. Ruiz, A. Yndart, V. Atluri, N. El-Hage, K. Khalili, M. Nair, *Sci. Rep.* **2016**, *6*, 25309.
- [29] T. Nguyen, J. Gao, P. Wang, A. Nagesetti, P. Andrews, S. Masood, Z. Vriesman, P. Liang, S. Khizroev, X. Jin, *Neurotherapeutics* **2021**, *18*, 2091.
- [30] A. Chaudhuri, K. Mandal, *J. Magn. Magn. Mater.* **2015**, *377*, 441.
- [31] N. D. Ferson, A. M. Uhl, J. S. Andrew, *IEEE Trans Ultrason Ferroelectr Freq Control* **2020**, *68*, 229.
- [32] J. Ghitman, E. I. Biru, R. Stan, H. Iovu, *Mater. Des.* **2020**, *193*, 108805.
- [33] A. R. Ahmed, O. C. Gauntlett, G. Camci-Unal, *ACS Omega* **2021**, *6*, 46.
- [34] F. S. L. Bobbert, S. Janbaz, T. van Manen, Y. Li, A. A. Zadpoor, *Mater. Des.* **2020**, 191.
- [35] J. Song, G. Zhu, H. Gao, L. Wang, N. Li, X. Shi, Y. Wang, *Bio-Des. Manuf.* **2018**, *1*, 254.
- [36] H. Song, M. A. Listyawan, J. Ryu, *Actuators* **2022**, *11*, 380.
- [37] G. V. Duong, R. Groessinger, M. Schoenhart, D. Bueno-Basques, *J. Magn. Magn. Mater.* **2007**, *316*, 390.
- [38] B. J. Rani, M. Ravina, B. Saravanakumar, G. Ravi, V. Ganesh, S. Ravichandran, R. Yuvakkumar, *Nano-Struct. Nano-Objects* **2018**, *14*, 84.
- [39] M. M. Vopson, Y. K. Fetisov, G. Caruntu, G. Srinivasan, *Materials* **2017**, *10*, 963.
- [40] K. L. Kozielski, A. Jahanshahi, H. B. Gilbert, Y. Yu, Ö. Erin, D. Francisco, F. Alosaimi, Y. Temel, M. Sitti, *Sci. Adv.* **2021**, *7*, eabc4189.
- [41] Y. Zhang, S. Chen, Z. Xiao, X. Liu, C. Wu, K. Wu, A. Liu, D. Wei, J. Sun, L. Zhou, H. Fan, *Adv. Healthcare Mater.* **2021**, *10*, e2100695.
- [42] J. Jang, C. B. Park, *Sci. Adv.* **2022**, *8*, eabn1675.
- [43] J. Kim, J. R. Staunton, K. Tanner, *Adv. Mater.* **2016**, *28*, 132.
- [44] L. V. Le, M. A. Mkrtschjan, B. Russell, T. A. Desai, *Biomed. Microdevices* **2019**, *21*, 43.
- [45] J. Venugopal, S. Low, A. T. Choon, S. Ramakrishna, *J Biomed Mater Res B Appl Biomater* **2008**, *84*, 34.
- [46] H. K. Makadia, S. J. Siegel, *Polymers* **2011**, *3*, 1377.
- [47] W. Jing, Y. Zhang, Q. Cai, G. Chen, L. Wang, X. Yang, W. Zhong, *ACS Chem. Neurosci.* **2019**, *10*, 348.
- [48] J. M. Aletta, *J Neurobiol* **1996**, *31*, 461.
- [49] M. L. Pall, *J. Cell. Mol. Med.* **2013**, *17*, 958.
- [50] D. J. Panagopoulos, A. Karabarbounis, L. H. Margaritis, *Biochem. Biophys. Res. Commun.* **2002**, *298*, 95.
- [51] S. Takemoto-Kimura, K. Suzuki, S.-I. Horigane, S. Kamijo, M. Inoue, M. Sakamoto, H. Fujii, H. Bito, *J. Neurochem.* **2017**, *141*, 808.
- [52] H.-S. Lee, S. I. Tomarev, *Exp. Cell Res.* **2007**, *313*, 98.
- [53] C. F. Blackman, J. P. Blanchard, S. G. Benane, D. E. House, *Bioelectromagnetics* **1994**, *15*, 239.
- [54] A. D. Rosen, *Cell Biochem. Biophys.* **2003**, *39*, 163.
- [55] G. Thrivikraman, S. K. Boda, B. Basu, *Biomaterials* **2018**, *150*, 60.
- [56] R. Liu, X. Huang, X. Wang, X. Peng, S. Zhang, Y. Liu, D. Yang, Y. Min, *Appl. Surf. Sci.* **2021**, *560*, 149965.
- [57] S. Meng, *Tissue Eng Regen Med* **2014**, *11*, 274.
- [58] R. Guduru, P. Liang, J. Hong, A. Rodzinski, A. Hadjikhani, J. Horstmyer, E. Levister, S. Khizroev, *Nanomedicine* **2015**, *10*, 2051.
- [59] M. A. Alvarez-Perez, V. Guarino, V. Cirillo, L. Ambrosio, *Biomacromolecules* **2010**, *11*, 2238.